OPEN ACCESS
IOP Publishing | International Atomic Energy Agency
Nuclear Fusion
Nucl. Fusion **66** (2026) 026010 (13pp)
https://doi.org/10.1088/1741-4326/ae27e5

Global tungsten erosion and migration modeling for the EU-DEMO with the ERO2.0 code

C. Baumann[1,*], J. Romazanov[1], D. Matveev[1], A. Kirschner[1], F. Subba[2], S. Wiesen[3], S. Brezinsek[1] and Ch. Linsmeier[1]

[1] Forschungszentrum Jülich GmbH, Institute of Fusion Energy and Nuclear Waste Management–Plasma Physics, 52425 Jülich, Germany
[2] NEMO Group, Politecnico di Torino, 10129 Torino, Italy
[3] DIFFER—Dutch Institute for Fundamental Energy Research, 5612 AJ Eindhoven, Netherlands

E-mail: c.baumann@fz-juelich.de

Received 29 September 2025, revised 18 November 2025
Accepted for publication 4 December 2025
Published 24 December 2025

Abstract

Global tungsten migration, thus erosion, transport, and deposition, in the EU-DEMO tokamak is investigated using ERO2.0 simulations for an argon-seeded ELM-free H-mode plasma scenario with expected 2 GW fusion power developed with the narrow-grid version of the SOLPS-ITER code. The tungsten erosion calculations by the plasma background include contributions from all ionic charge states of deuterium, helium, and argon, as well as deuterium charge-exchange neutrals. The latter is estimated in the framework of advanced kinetic energy spectra recorded at various poloidal locations across the device. Since the SOLPS-ITER plasma solution demands an extrapolation of plasma parameters up to first wall panels made of tungsten, different assumptions on the far-SOL plasma temperature profiles ranging from 2 eV to about 10 eV are applied in order to study their impact on tungsten erosion and transport on EU-DEMO. The simulations reveal that main chamber erosion is dominated by charge-exchange neutrals for very cold far-SOL conditions of 2 eV, while it is driven by argon ions and tungsten self-sputtering when going to higher temperatures. This is different for the semi-detached divertor, where the erosion is clearly dominated by argon ions in all cases. The ratio between divertor to main chamber source is found to decrease from roughly 10 to 3 with increasing far-SOL temperature. A net main chamber to divertor transport of tungsten is observed and explained by long ionization mean free paths of sputtered tungsten atoms, ranging from 50% and 39% for the applied $[T_e, T_i]$ far-SOL assumptions.

Keywords: EU-DEMO, plasma–wall interaction, erosion-deposition, plasma impurity migration, ERO2.0 code

(Some figures may appear in colour only in the online journal)

* Author to whom any correspondence should be addressed.

1. Introduction

The understanding and control of plasma–wall interaction (PWI) in magnetic fusion devices is essential for their safe and long-term operation. While the erosion of plasma-facing components (PFCs) by physical and, in some cases, chemically assisted sputtering impacts their lifetime, the deposition of eroded material may cause dust formation and lead to increased retention via co-deposition of fuel isotopes, which in turn can become critical in terms of safety and fuel cycle reasons. Numerical modeling of such processes is thus inevitable not only to gain more detailed insights into experiments in present day machines, but also to make predictions for future machines. Steady-state PWI can be assessed for instance with the Monte Carlo codes ERO [1] and its successor ERO2.0 [2]. Due to its massive parallelization, the latter allows for simulations of full reactor-scale geometries. Both codes calculate the erosion under ion and charge-exchange neutral (CXN) impact with subsequent tracing of eroded impurities through the scrape-off layer (SOL) plasma. Along the trajectory, atomic processes like ionization, recombination, and Coulomb collisions with the background plasma ions are considered. The ERO2.0 code has been validated against experimental data from the already stop of operating fusion device JET with the focus on beryllium (Be) [2, 3] and tungsten (W), as applied PFC material [4]. In addition, predictions have been made for the next step device ITER [5–7], which is currently under construction in France. In parallel to ongoing work on ITER, there are already efforts in Europe to advance the fusion roadmap towards a demonstration fusion power plant referred to as EU-DEMO [8, 9]. In particular, the development and validation of high-performance computer codes in view of their application to next step fusion devices has been bundled within the EUROfusion Theory and Advanced Simulation Coordination [10] activities. The main aim of one of the projects within these activities comprises the assessment of safety-relevant information regarding fuel inventory, dust production, and lifetime of PFCs in order to support the EU-DEMO conceptual design. ERO2.0 modeling builds the basis for predictive PFCs erosion and deposition estimates and the present work reports a first comprehensive study in this regard. However, it is noted that the study should be seen as a first step towards reliable predictions in the future due to various reasons in terms of magnetic equilibrium and plasma background, which are discussed later on. Therefore, the paper is organized as follows: section 2 gives information on the modeling set-up. This includes a discussion about the underlying magnetic equilibrium, the plasma scenario, and the transport assumptions used in the modeling. Steady-state erosion and deposition maps for the EU-DEMO tokamak can be found in section 3. Finally, section 4 draws a conclusion on the presented ERO2.0 modeling.

2. Simulation set-up

2.1. Wall geometry

The ERO2.0 modeling considers the realistic three-dimensional geometry of the EU-DEMO tokamak design 2017 and was provided by the DEMO Central Team [11] in the form of a polygonal surface mesh. In more detail, the divertor is represented by $\sim$18, 000 quadrilateral polygons. Each polygon has side lengths of about 3 cm. The first wall geometry is divided into $\sim$300, 000 triangular polygons with side lengths of 5 cm. Sacrificial first wall limiters are omitted for the beginning (see figure 6 in [12] to get a full list of these limiters), since they go beyond the scope of the present study of establishing an initial workflow of ERO2.0 modeling for EU-DEMO. Simultaneously, the neglection of sacrificial limiters has the advantage of increasing the rotational symmetry of EU-DEMO by a factor of 4 (from 4-fold to 16-fold rotational symmetry), so that only a unique sector of 22.5° in combination with periodic boundary conditions is sufficient to model the full torus device. This is preferable in terms of Monte-Carlo statistics and computation time. Finally, the entire wall surface is assumed to be made of W.

2.2. Magnetic equilibrium

The magnetic equilibrium is a mandatory input for migration studies with the ERO2.0 code. In particular, the start of flat-top (SOF) phase of the 2017 EU-DEMO Baseline scenario [13] is used in the modeling. The reason for using the 2017 Baseline is due to the fact that only for this scenario a complete lower single-null plasma solution was available at the start of the present studies [14]. The modeling presented here is thus not to be considered as predictive for the full power EU-DEMO operation, but should be seen as a preparation for ERO2.0 applications in yet unexplored regimes in terms of machine size, plasma to wall gap and so on.

The magnetic configuration used throughout the present study is shown in figure 1, where selected flux surfaces are plotted (grey solid curves) together with the local direction of the poloidal magnetic field (grey arrowheads). The separatix is highlighted as green solid curve. In addition, the plot reveals the presence of a secondary X-point at the top the machine, which is (magnetically) connected to the horizontal tops of the divertor on both the high- and on the low-field side. The toroidal magnetic field points towards the reader and has a strength of $B_t \approx 4.89$ T evaluated at the plasma center at $R \approx 8.94$ m (not shown in the figure). The plasma current is $I_p \simeq 19$ MA.

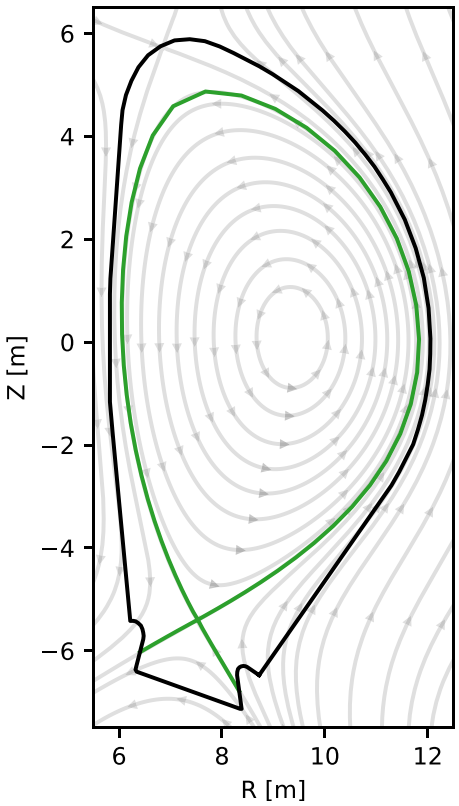

Figure 1. Contour plot of selected magnetic flux surfaces for the start of flat-top 2017 Baseline equilibrium. The arrows show the direction of the poloidal magnetic field. The toroidal magnetic field points out of the plane towards the reader. The green and black curves show the separatrix and the contour of the most protruding part of the wall panels of EU-DEMO, respectively.

ERO2.0 has its own built-in capability to perform magnetic shadowing calculations for shaped wall panels. Such a calculation is based on the connection length, which equals the distance between two points on the wall, measured along a magnetic field line connecting these two points[4]. For main chamber panels in EU-DEMO representing *breeding blankets*, the resulting connection lengths are shown in figure 2(*a*). In general, there are several models to relate the magnetic shadowing factor S to the local value of the connection length. One of the simplest models is used here, in which S can only take values of 0 or 1. In particular, a surface cell will be magnetically shadowed, i.e. $S = 0$, if the connection length is shorter than or equal to a certain threshold value L_{th}. Otherwise, the surface cell will be plasma wetted ($S = 1$). In the present case, L_{th} is set to 6 m, which was also assumed in corresponding ERO2.0 calculations for ITER [5]. The resulting shadowing pattern for the EU-DEMO main chamber wall is given in figure 2(*b*), where dark blue patterns indicate plasma-wetted regions. Due to its high degree of toroidal symmetry, the entire divertor is assumed to be plasma wetted, so that $S = 1$ holds for all divertor surface cells.

2.3. Plasma background

In addition to the magnetic configuration, information about plasma parameters in the boundary region is needed. This includes in particular the electron density n_{e}, electron and ion temperature T_{e} and T_{i}, the background flow velocity parallel to the magnetic field v_{par}, as well as the density distribution of seeding impurities. The plasma background is important for the calculation of the erosion source due to impinging ion fluxes onto the wall, but it also impacts the migration part of ERO2.0, where it enters into the calculation of atomic processes (ionization and recombination) and collisions of traced impurities with the background plasma species. The accuracy of any ERO2.0 modeling is therefore strongly coupled to the quality of the background.

For the present work, the lower single-null ELM-free H-mode SOLPS-ITER plasma solution for EU-DEMO with expected 2 GW fusion power is used [14], which describes a deuterium (D) plasma with helium (He) ash and argon (Ar) as seeding species for divertor radiation. Tritium is not accounted for in the SOLPS-ITER plasma solution. However, it is the first time that the full distribution of seeding impurities from a plasma edge code is used within an ERO2.0 modeling. This replaces the constant background concentration approach, where ions belonging to species α could only be included as a spatially constant fraction c_α measured with respect to the background electron density $n_\alpha = c_\alpha n_{\mathrm{e}}$. In general, the impurity background is required in order to include particle collisions in the Fokker-Planck term for impurity transport[5] and to calculate the erosion source at the wall. It is important to note that both are handled in a different manner. With regard to particle collisions, i.e. in the plasma volume, an effective background characterized by the effective mass

$$m_{\mathrm{eff}} = \frac{\sum_\alpha m_\alpha n_\alpha}{\sum_\alpha n_\alpha}, \tag{1}$$

the effective charge

$$Z_{\mathrm{eff}} = \frac{\sum_\alpha q_\alpha^2 n_\alpha}{n_{\mathrm{e}}}, \tag{2}$$

and the effective parallel flow velocity

$$v_{\mathrm{eff}}^{\mathrm{par}} = \frac{\sum_\alpha v_\alpha^{\mathrm{par}} n_\alpha}{\sum_\alpha n_\alpha} \tag{3}$$

is used with m_α, q_α, and v_α^{par} representing the individual mass, charge and parallel flow velocity of species α, respectively. In contrast, the contribution of each species is considered individually at first wall surfaces to get the erosion source. Therefore, the impinging ion flux onto the wall is calculated as

$$\Gamma_\alpha = n_\alpha \cos(\theta_B)\, c_{\mathrm{eff}}^s S, \tag{4}$$

[4] A benchmark of ERO2.0 results against PFCFlux [15] simulations has shown very good agreement, but will be published elsewhere.

[5] Collisional ionization is only driven by electrons in the ERO2.0 code.

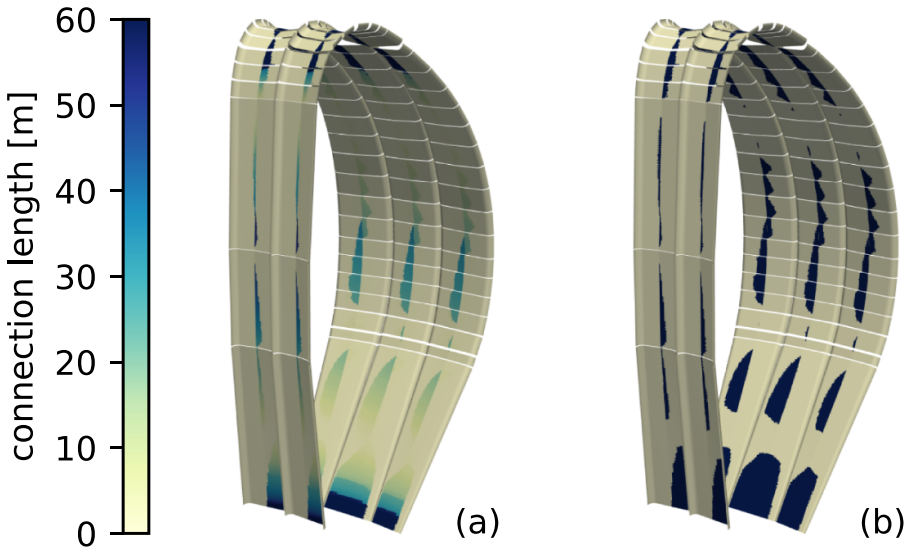

Figure 2. Plot of (*a*) the connection length and (*b*) the magnetic shadowing factor. For the latter, dark blue regions indicate plasma-wetted areas, where the magnetic shadowing factor is equal to $S = 1$.

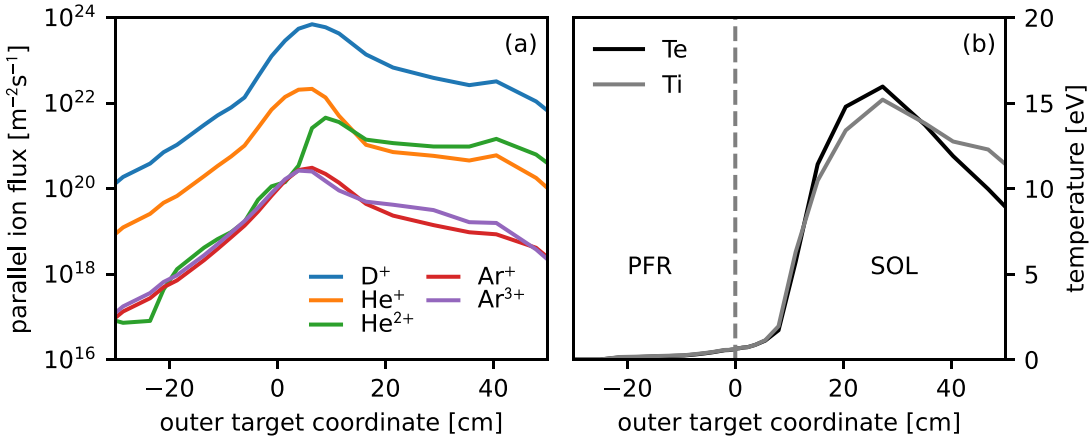

Figure 3. Plot of (*a*) selected ion flux and (*b*) temperature profiles along the outer target up to the divertor top. Positive target coordinates describe the SOL, negative ones the PFR.

where θ_B is the magnetic inclination angle, c^s_{eff} is the common ion sound speed for the multi-species background [16, 17],

$$c^s_{\text{eff}} = \sqrt{\frac{\sum_\alpha n_\alpha \left(k_B T_\text{i} + q_\alpha k_B T_\text{e}\right)}{\sum_\alpha n_\alpha m_\alpha}}, \tag{5}$$

and S is the shadowing factor introduced in section 2.2. The assumption of a common ion sound speed for all background species is in agreement with the boundary conditions imposed in the SOLPS-ITER modeling [14]. Selected ion flux profiles along the outer divertor target are shown in figure 3(*a*). The profiles show that the constant concentration assumption is inappropriate. One can see that the relative concentrations change especially in the SOL region of the target (indicated by positive target coordinates). While lower-ionized states (He^+ and Ar^+) are dominant close to the strike-point, there is a qualitative change roughly 15 cm into the SOL, where higher-ionized states tend to dominate (He^{2+} and Ar^{3+}). This can be explained by the semi-detached solution with a pronounced temperature rise towards the outer divertor baffle reaching peak temperatures of $T_\text{e} \approx T_\text{i} \approx 16$ eV (see figure 3(*b*) and [14]). Since the ion impact energy depends on the particle's charge q via the sheath acceleration [18], $\langle E \rangle = 2k_B T_\text{i} + 3qk_B T_\text{e}$, and the sputtering yield depends on the particle's impact energy at the surface, the charge-state resolved fluxes thus improve the calculation of the ion background-induced erosion source significantly.

Unfortunately, the aforementioned improvement is counteracted by the following. The plasma solution is limited to the domain of the B2-part of SOLPS-ITER, which does not cover the entire boundary region up to the first wall. This is illustrated in figure 4 where the B2-grid is shown in grey and the 2D contour of the EU-DEMO wall geometry in black. One can see that the B2-grid covers the wall only along the divertor targets. Void spaces between the grid and the wall can be observed in all other parts of the machine. In more detail, the distance of the last B2-grid cell to the first wall measures ∼8 cm at the inner mid-plane, ∼15 cm at the outer mid-plane, ∼60 cm at the

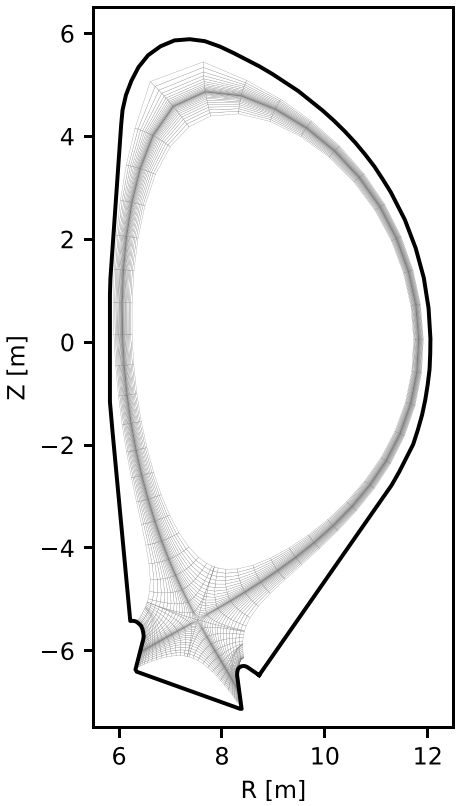

Figure 4. Plot of the B2-grid (grey) together with a 2D contour of the EU-DEMO wall geometry (black).

top of the machine, and even up to ∼80 cm above outer divertor baffle. For the ERO2.0 modeling, this makes an extrapolation of plasma parameters necessary, which simultaneously introduces large uncertainties, since the final plasma conditions at the wall strongly depend on the assumptions made for the extrapolation. In the following, an

- exponential decay for densities, $n(d) = n_0\, e^{-d/\lambda}$,
- exponential decay for temperatures, $T(d) = T_0\, e^{-d/\lambda}$,
- flat extrapolation for the Mach number, $M(d) = M_0$,

is assumed, where d is the distance of a point outside the grid to its projection point on the outermost B2-ring, $\lambda = 5\,\mathrm{cm}$ is the constant decay constant, and zero-indexed parameters correspond to their respective values at the projection point. It is further noted that temperatures in the far-SOL main chamber plasma boundary are capped at a certain T_{min}, which will lead to flat temperature profiles in the far SOL. Similar assumptions have been made within an onion-skin model used to extend narrow-grid SOLPS simulations towards the first wall in ITER before [19] and can be regarded as conservative in view of W sputtering considering shoulder formation by turbulence. For the present study, different values of T_{min} will be discussed later, which are set to lower values as compared to the ITER-case, where $10\,\mathrm{eV} < T_{\mathrm{e}} < 20\,\mathrm{eV}$ and $20\,\mathrm{eV} < T_{\mathrm{i}} < 40\,\mathrm{eV}$ to be in line with the very conservative ITER heat load specifications. On the B2-grid, the Mach number is determined as $M = v_{\mathrm{eff}}^{\mathrm{par}}/c_{\mathrm{eff}}^{s}$. As an example, inner mid-plane profiles for the electron density n_{e}, electron temperature T_{e}, and the local Mach number are given in figure 5 for the case $T_{\mathrm{min}} = 2\,\mathrm{eV}$. At the inner mid-plane, the distance between the B2-grid and the wall reaches with roughly 8 cm its minimum for the entire main chamber, so that the shortest space has to be bridged. However, one can see that even here the electron temperature T_{e} will be capped at 2 eV close to the wall apex, which means that electron and ion temperature (not shown here) are constant along the main chamber wall, $T_e^w = T_i^w = 2\,\mathrm{eV}$. As a result, erosion of the main chamber wall by D ions under such low-temperature conditions is negligible as D ion impact energies of order 10 eV are well below the W sputtering threshold of about 250 eV for a constant impact angle of 60° with respect to the surface normal (see figure 6), which is used in the modeling for all projectiles from the background and has been shown in the past to be a good approximation even for rough surfaces [20, 21]. The situation is different for heavier species such as Ar, for which the sputtering threshold is roughly 40 eV. That value can be exceeded especially by higher ionized charge states, so that Ar ions are expected to give a finite contribution to the W erosion source. An even lower threshold is observed for W self-sputtering. Here, it is important to stress that W and re-deposited W are assumed to behave identically. Thus, enhanced re-erosion due to weakened surface binding of re-deposited W is not considered in the present study though corresponding evidence has been reported for experiments in TEXTOR equipped with carbon PFCs [22].

2.4. CXNs

The erosion induced by D CXNs is in some aspects different compared to ions: on the one side, CXN can reach magnetically shadowed areas of the machine as they are not bound to magnetic field lines. This leads to almost toroidally symmetric erosion patterns in contrast to ions, where the erosion pattern is mainly restricted to plasma-wetted areas. On the other side, the energy of a D CXN is mostly decoupled from the (far-)SOL conditions and rather depends on the conditions within the pedestal region, where the conversion of hot D ions into energetic neutrals via charge-exchange collisions takes place. This allows sputtering by high-energy D CXNs to become the dominant mechanism in low-temperature SOL conditions, which is especially pronounced for full W devices due to the strong dependence of the sputtering yield on the impact energy. Consequently, detailed information about the energy distribution of CXNs at the wall is decisive in order to compute the erosion source accurately. In the present work, full kinetic energy spectra of D CXNs obtained via standalone EIRENE [24] simulations on basis of the SOLPS-ITER background are therefore used. In particular, energy spectra at 12 different poloidal locations across the torus have been recorded for EU-DEMO, which are marked in figure 7(*a*). Each spectrum is sampled into 2000 energy bins and ranges up to a maximum energy of 10 keV. Four example spectra are shown in figure 7(*b*). It is further noted that each colored curve refers to the corresponding marker color in figure 7(*a*). Each spectrum can be associated with an effective sputtering yield by simply convoluting the sputtering yield with the spectral

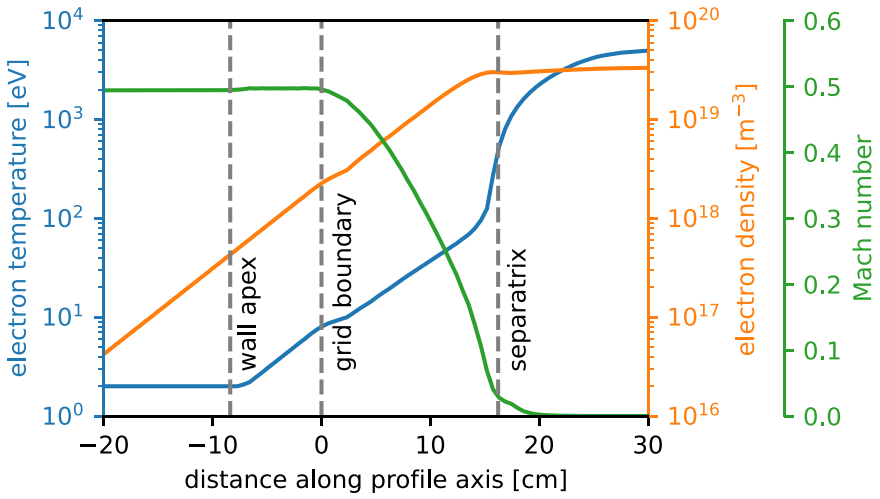

Figure 5. Inner mid-plane profiles of the electron temperature (blue), electron density (orange), and Mach number (green). The electron temperature is capped at $T_{\min} = 2\,\mathrm{eV}$. The dashed lines indicate the wall apex and the separatrix. The B2-grid boundary is located at zero distance. Negative distances describe the region, where the plasma parameters are extrapolated.

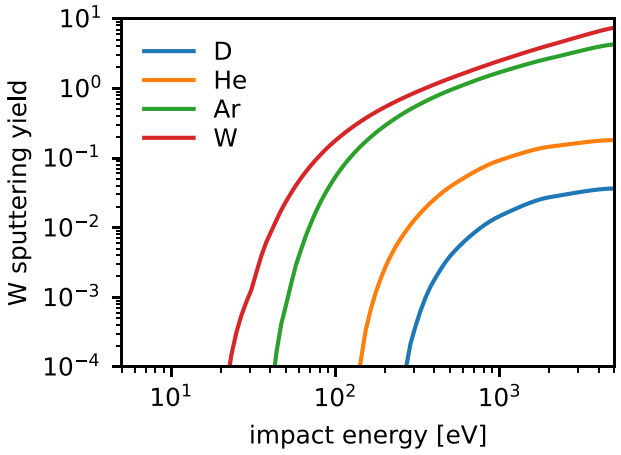

Figure 6. Dependence of the physical sputtering yield on the impact energy for different projectiles impinging on a W target at a constant impact angle of 60° measured with respect to the surface normal. The ERO2.0 database was compiled using SDTrimSP version 6.01 [23].

distribution function $f(E)$,

$$Y_{\mathrm{eff}} = \int \mathrm{d}E\, Y(E) f(E)\,, \tag{6}$$

where similar to background ions a constant impact angle of 60° is used as reasonable approximation even for rough surfaces. The effective sputtering yield at any location on the wall is then determined by linear interpolation of the two closest effective sputtering yields, which are weighted by their distance to the wall location of interest. In doing so, figure 8 shows a poloidal profile of the effective sputtering yield obtained for the spectral approach (grey curve).

In addition, figure 8 also shows the effective yield for the mean energy approach. This is typically the standard option in ERO2.0 if kinetic energy spectra are not available and it was used earlier for Be-covered surfaces [5, 7] as well as for W-covered surfaces including a full-W ITER as a proxy for EU-DEMO [25] and prior modeling for EU-DEMO itself [26]. In this method, the sputtering yield is determined under the assumption that all neutrals impact the wall with a mono-energetic energy distribution defined by their local mean energy, $Y_{\mathrm{eff}} = Y(\langle E \rangle)$. The required poloidal profile of the mean energy is a standard EIRENE output, and the profile for the EU-DEMO case can be found in figure 7(*c*) (black curve). A comparison of both approaches reveals two main results: On the one side, the peak value of Y_{eff} is lower by a factor of about 2.5 in the full energy spectra approach, at least under the present conditions. On the other side, figure 8 reveals the emergence of additional W sources due to sputtering. While the W source is mainly localized around the outer mid-plane in the mean energy approach, the full energy spectra approach in contrast predicts a broader region, thereby covering almost the entire wall on the low-field side. A weak(er) W source is also estimated on the high-field side. The aforementioned emphasizes the importance of proper treatment of CXN-induced erosion in order to assess safety-relevant information with regard to the erosion of PFCs.

2.5. Transport model

In the present work, the tracing of W impurities throughout the plasma background is simulated in the adaptive guiding-center approximation (aGCA). In this approach, the gyro orbit is only resolved in areas of special interest like for instance in the vicinity of the wall in order to calculate the W impact parameters as accurate as possible. In all other regions, the pure GCA algorithm is used to speed up the computation. A detailed description of the ERO2.0 implementation together with selected benchmark tests can be found in [27].

Along the trajectory, collisions of W impurities with the plasma background are considered in the Fokker-Planck framework as described by Reiser *et al* [28]. However, it has to be noted that the collision operator is prone to numerical

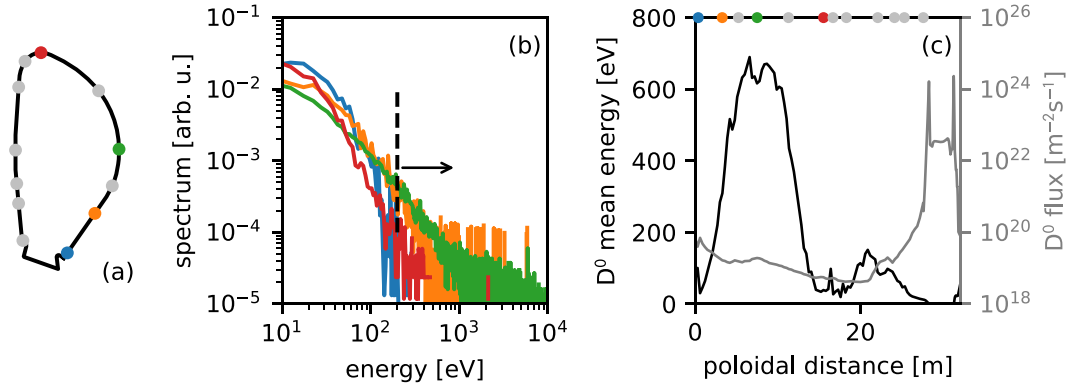

Figure 7. (*a*) Visualization at which locations kinetic energy spectra from dedicated EIRENE simulations are recorded. (*b*) Log-log plot of selected D^0 energy spectra. The color of each curve refers to the marker color in subplot (*a*). Each spectrum is normalized such that the integral is unity. The black dashed line indicates the D $\rightarrow$ W sputtering threshold. (*c*) Poloidal profiles of the D^0 mean energy (black) and the total D^0 flux at the wall (grey).

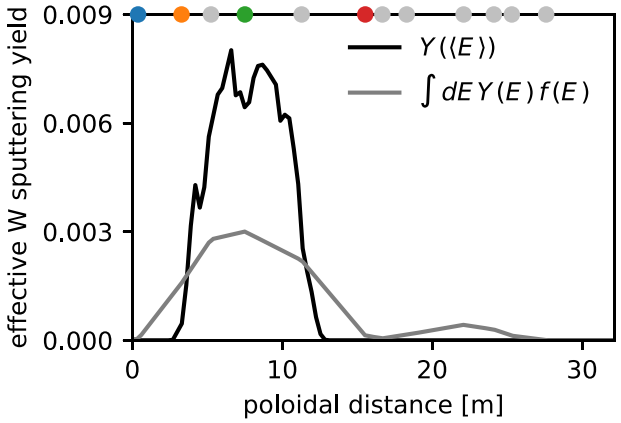

Figure 8. Poloidal profiles of the effective sputtering yields for the mean energy approach (black curve) and the full spectral approach (grey curve). In both cases, the impact angle is assumed to be 60°.

divergence under certain conditions. For instance, the collision of W impurities with a cold, but dense plasma background (i.e. conditions along the strike-lines) has been identified to lead to the acceleration of the W particles up to MeV energies in early scoping studies with the ERO2.0 code. The reason for the numerically unstable behavior could be attributed to locally ultra-short Spitzer collision times τ_{coll}, which become shorter than the global timestep Δt_0 used for the particle tracing. In principle, the issue can be triggered within both the full gyro-orbit tracing mode and the GCA tracing mode. However, it is observed much earlier in the GCA mode, because of the larger timesteps applied (typically 50 ns to 100 ns). The issue disappears inherently once the tracing timestep is set to resolve the shortest Spitzer time in the system, $\Delta t_0 \ll \tau_{\mathrm{coll}}$. Unfortunately, this may come along with a significant performance drop, since Δt_0 is generally small enough for the vast majority of plasma background parameters. In ERO2.0, a different approach is therefore utilized. Instead of reducing the global timestep, only collision processes for unstable conditions are treated with a reasonably short timestep Δt_{coll}, thereby however repeating the collision process N times, where N is chosen such that the collision is well resolved. Test simulations have shown that the procedure removes the divergence of the collision operator with reasonable accuracy and acceptable performance losses. It is noted that the same issue has been observed independently in EIRENE's kinetic ion tracing module, where it has been fixed with the introduction of an adaptive timestep model [29].

Thermal force effects [30, 31] on the W transport are neglected in the present study, which may lead to an underestimation of W escaping poorly screened divertor surface areas [4]. Refined ERO2.0 simulations are currently in progress and will be published elsewhere. In addition, anomalous cross-field diffusion is modeled in terms of a spatially constant diffusivity coefficient which is set to $D_\perp = 1\,\mathrm{m^2\,s^{-1}}$. In general, spatially resolved diffusivity coefficients can be imposed in ERO2.0 [4], which will be one of the next improvements for modeling the EU-DEMO tokamak.

3. Modeling results

The following sections report on the ERO2.0 modeling results for three different assumptions on the far-SOL temperature cutoffs, which are 2 eV, 5 eV, and flat temperature profiles from the last available flux surface towards the first wall. Typically, the latter results in electron temperatures below 8 eV and ion temperatures around 10 eV.

3.1. Far-SOL temperature 2 eV

Main chamber erosion and redeposition profiles are shown in figure 9. In particular, separate erosion profiles are shown for each contributing species. A peak main chamber gross erosion flux of about $\Gamma_{\mathrm{gross}}^{\mathrm{max}} \simeq 9.31 \times 10^{17}\ \mathrm{m^{-2}s^{-1}}$ is predicted on the inner side of the wall, which can be attributed to sputtering by Ar ions. Though Ar ions cause the peak gross erosion flux, significant gross erosion is only expected in a small area on the inner side of the machine around the mid-plane (see figure 9(*b*)). The integration of the gross erosion flux over the main chamber surface area yields a

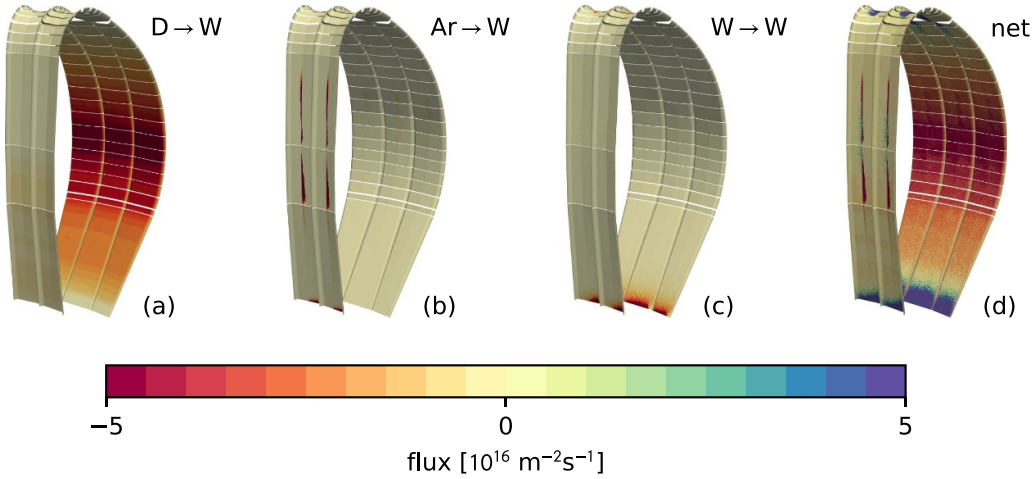

Figure 9. Tungsten main chamber ((*a*)–(*c*)) gross and (*d*) net erosion. The gross erosion is divided into the contributing species (*a*) D^0 and D^+, (*b*) Ar ions, and (*c*) W self-sputtering. Positive values (shades of green and blue) indicate deposition, negative values (shades of red) indicate erosion. The far-SOL main chamber temperature is 2 eV.

release of $R^{\text{gross}}_{\text{Ar}\to\text{W}} \simeq 2.01 \times 10^{18}$ W-atoms s^{-1} due to sputtering by Ar ions (see table 1). In contrast, significant erosion by D can be found almost along the entire outer wall of the machine (see figure 9(*a*)). The torodially symmetric shape of the erosion map underlines that erosion is dominated by CXN, which can reach even recessed and magnetically-shadowed areas on the wall. Though the corresponding peak erosion flux is smaller by a factor 17 in comparison to Ar, the total number of W atoms released by D sputtering is 14 times higher ($R^{\text{gross}}_{\text{D}\to\text{W}} \simeq 27.58 \times 10^{18}$ W-atoms s^{-1}, see table 1). In fact, D CXN sputtering releases more than 85% of all W atoms in the main chamber in case of $T_\text{e} = 2$ eV in the far SOL. Figure 9(*c*) shows the contribution of W self-sputtering under the assumption that W and re-deposited W behave identically as mentioned before. Additionally, it is noted that no specific assumptions on W impact energy and impact angle at the wall (as a reminder, $\langle E_\text{in}\rangle = 2k_BT_\text{i} + 3qk_BT_\text{e}$ and $\theta_\text{in} = 60°$ for all background projectiles) are needed as they are inherently included in ERO2.0 as a result of the W impurity tracing throughout the plasma background. The simulation predicts W self-sputtering to be strongest in the lower part of the low-field side above the outer divertor baffle. There is an additional contribution at the top of the device, which is hardly visible on the applied color scale. In total, the surface-integrated self-sputtering rate in the main chamber is $R^{\text{gross}}_{\text{W}\to\text{W}} \simeq 1.84 \times 10^{18}$ W-atoms s^{-1}, which is similar to the Ar result (see table 1). Finally, the net W erosion flux is shown in figure 9(*d*), where reddish colors indicate net erosion while bluish ones refer to net deposition. Surface areas eroded by the plasma background (i.e. by D CXN and Ar ions) remain also net erosion zones. This is different for areas in which W self-sputtering is dominant, which turn into net deposition zones instead. For instance, there is strong net deposition at the lower part of the low-field side wall and at the top of the machine close to the secondary X-point (see figure 1).

The modeling predicts that the transport of W impurities strongly depends on the location of the W source. This can be seen in the reduced transport matrix depicted in figure 10,

Table 1. Surface-integrated W erosion rates for a far-SOL main chamber temperature of 2 eV. Positive and negative values for the dataset *net* denote net deposition and net erosion, respectively. It is noted that W erosion by D is dominated by CXNs.

(10^{18} atoms s^{-1})	net	gross	D → W	Ar → W	W → W
Main chamber	-12.85	31.43	27.58	2.01	1.84
Divertor	11.69	318.56	—	248.59	69.96

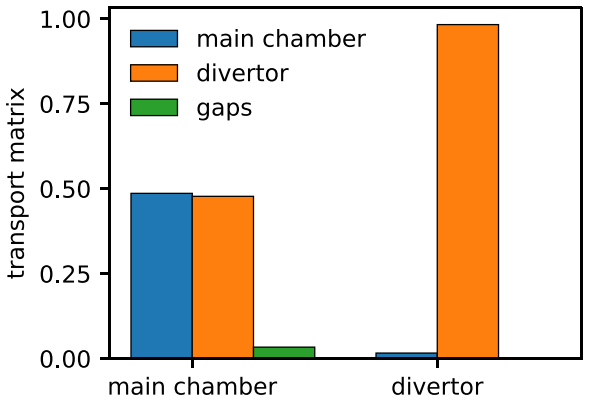

Figure 10. Plot of the reduced transport matrix. The *x*-axis refers to the PFCs, where the particles started. The different bars show the relative amount of particles deposited on the corresponding PFC (or are lost to poloidal gaps).

which illustrates the probability (*y*-axis) of W transport from the *erosion* PFC (*x*-axis) to the *deposition* PFC (colored bars). For example, almost no relative transport from the divertor to the main chamber is observed, indicating efficient divertor screening. In contrast, there is significant W transport from the main chamber into the divertor. In particular, almost 50% of W eroded in the main chamber is deposited somewhere in the divertor. Qualitatively, strong W transport into the divertor deviates from observations in prior PWI modeling for a full-W ITER conducted with both the ERO2.0 code (between 1%

and 2% are stated in [25] depending on the magnetic configuration) and the WallDYN code (see figure 2(b) in [32]). It is the assumed far-SOL plasma conditions that drive this change. The assumptions made for EU-DEMO correspond to a cold and thin far-SOL plasma, which causes long ionization mean-free paths of W atoms. Conversely, higher far-SOL temperature values compared to EU-DEMO ranging between 10 eV and 20 eV for electrons and 20 eV and 40 eV for ions are assumed on ITER, so that W atoms are ionized on outer flux tubes magnetically not connected to the divertor. From a quantitative point of view, the observed transport patterns seem to be less severe due to the large ratio of divertor to main chamber W source. In particular, the divertor source is 10 times stronger than the main chamber W source assuming 2 eV far-SOL temperatures. Finally, figure 10 also shows that roughly 3% of W particles are lost in poloidal gaps between first wall panels.

3.2. Far-SOL temperature 5 eV

In order to quantify the impact of the far-SOL temperature assumptions on the modeling, additional simulations were conducted. The present section considers the case, where the far-SOL electron and ion temperatures in the main chamber are capped at an increased value of $T_{\mathrm{min}} = 5\,\mathrm{eV}$ with respect to the reference case. Similar to the colder far-SOL case shown before, both the electron and ion temperature are constant along the main chamber first wall, but still too low for W sputtering by D ions. In addition, also the D-CXN contribution is unchanged (see table 2), because the far-SOL plasma conditions are not taken into account in the standalone EIRENE modeling performed in order to obtain the energy spectra at different wall locations (see discussion in section 2.4). However, this lack of self-consistency is not expected to change the results much since the CXN energy distributions are determined by the hot core plasma rather than by the cold (far-)SOL; and it will be absent in future extended-grid SOLPS-ITER/EIRENE modeling that covers the entire plasma boundary up to the wall [33]. Quantitatively, the contributions by Ar ions and by W self-sputtering in contrast are increased. For instance, the peak gross erosion flux induced by Ar ions increases by a factor of ∼6 to $\Gamma^{\mathrm{max}}_{\mathrm{gross}} \simeq 5.53 \times 10^{18}$ $\mathrm{m^{-2}s^{-1}}$, while the total Ar-related W main chamber source increases even by a factor ∼13, $R^{\mathrm{gross}}_{\mathrm{Ar}\rightarrow\mathrm{W}} \simeq 25.64 \times 10^{18}$ W-atoms $\mathrm{s^{-1}}$, thereby almost replacing D-CXN as the biggest contributor[6]. The W self-sputtering source is stronger by a factor ∼5. Combining all separate contributions, it yields a twice as large main chamber W gross source in comparison to the reference case. Qualitatively, one can see significant W sputtering by Ar ions on the low-field side around the outer mid-plane, see figure 11(*a*). In addition, figure 11(*b*) shows that W self-sputtering becomes more pronounced at the top of the machine and on the high-field side around the inner mid-plane. Interestingly, the erosion patterns induced by W self-sputtering do not correlate with the patterns by plasma ion sputtering.

[6] It should be noted a factor of $\sqrt{(5/2)} \approx 1.6$ is related to increasing ion fluxes onto the first wall as a result of the scaling of the sound ion speed (see equations (4) and (5)); the rest comes from more efficient sputtering as a result of higher ion impact energies.

Table 2. Surface-integrated W erosion rates for a far-SOL main chamber temperature of 5 eV. Positive and negative values for the dataset *net* denote net deposition and net erosion, respectively. It is noted that W erosion by D is dominated by CXNs.

(10^{18} atoms $\mathrm{s^{-1}}$)	net	gross	D → W	Ar → W	W → W
Main chamber	–24.70	63.17	27.58	25.64	9.96
Divertor	21.13	341.21	—	253.93	87.27

The W net erosion map is given in figure 11(*c*). Similar to the case before, one can see that areas of significant background sputtering stay net erosion zones, while areas with significant W self-sputtering turn into net deposition zones. The strong decoupling between net erosion and net deposition is correlated to the previously mentioned W transport patterns. Though the transport matrix for the present far-SOL temperature assumption (not shown as a separate figure) shows a slight reduction of W transport into the divertor, it is still relatively large with about 42% of W particles re-deposited very non-locally. Physically speaking, the increase from 2 eV to 5 eV therefore does not alter the transport much. This is indeed reasonable as the lowest ionization potential $I^{\mathrm{W}}_{\mathrm{pot}}$ of W equals 7.86 eV [34], so that the ionization dynamics is similar in both scenarios.

The divertor target conditions do not depend on the far-SOL temperature assumptions, because the plasma grid in the SOLPS-ITER simulation extends up to the wall. In fact, this does not apply to the horizontal parts at the top of the divertor as can be seen in figure 4. As a consequence, the corresponding surface areas at the top of the divertor together with the plasma volume above are located in the extrapolation domain. This in turn causes a weak dependence on the far-SOL temperatures and leads in the present case to a slight increase in the W gross erosion by Ar ions. Tungsten self-sputtering also becomes more important due to higher influx from the main chamber. However, as the increase of the divertor W source with increased far-SOL temperature is only moderate, the relative impact of the main chamber W source gains in importance. For instance, the ratio of divertor to main chamber W gross source drops from roughly 10 to 5 while increasing the far-SOL temperature from 2 eV to 5 eV.

3.3. Far-SOL temperature: constant extrapolation

The next logical step is the assumption of far-SOL temperatures well beyond the ionization potential of W in order to trigger more pronounced changes in the W transport. Unfortunately, the options to further increase T_{min} are limited, which can be seen in figure 12, where profiles of the electron (blue solid curve) and ion temperature (orange solid curve) along the last poloidal main chamber flux tube for the considered SOLPS-ITER plasma background are depicted together with the first ionization potential of W (black dashed line). One can see that the electron temperature only exceeds the first ionization potential of W on the high-field

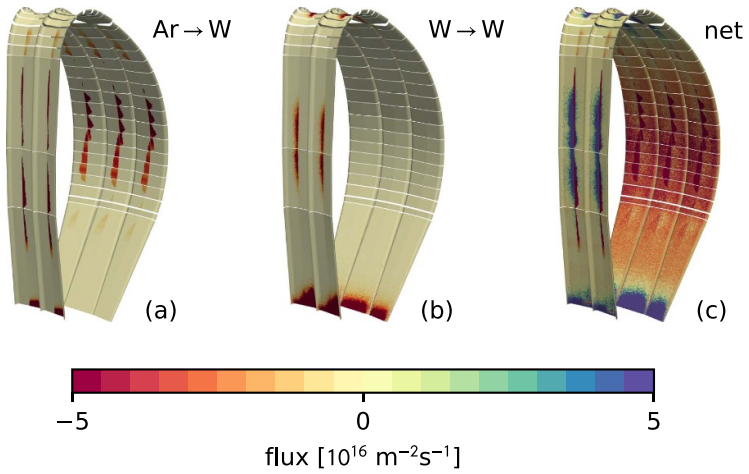

Figure 11. Tungsten main chamber ((*a*) and (*b*)) gross and (*c*) net erosion. The gross erosion is divided into the contributing species (*a*) Ar ions and (*b*) W self-sputtering. Positive values (shades of green and blue) indicate deposition, negative values (shades of red) indicate erosion. The far-SOL main chamber temperature is 5 eV.

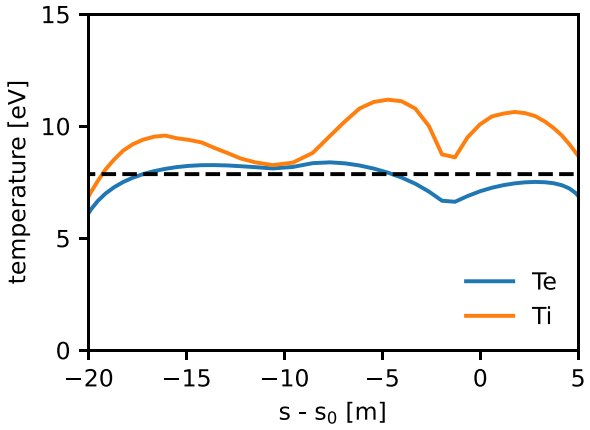

Figure 12. Poloidal profiles of the electron (blue) and ion temperature (orange) along the last main chamber flux tube available on the SOLPS-ITER grid. The black dashed line shows the first ionization potential of W at 7.86 eV. The poloidal coordinate is given in reference to the value at the outer mid-plane s_0.

side of the machine. Since ionization is due to electron impact, it is governed by the electron temperature profile. However, an assumption of T_e above 7.68 eV in the main chamber far-SOL would lead to a sudden and discontinuous increase of the electron temperature towards the wall in some areas of the machine. In order to avoid this, flat temperature profiles from the last flux tube towards the wall, i.e. a constant extrapolation, are therefore imposed as most suitable option to enter a different ionization regime with respect to the previous cases. Simultaneously, this can be regarded as worst-case scenario for the present plasma background in terms of plasma temperature conditions at the wall.

From a quantitative point of view, there is a change in the main contributors for the main chamber source. In particular, the relative contributions for D, Ar, and W are 22%, 54%, 24%, respectively (see table 3). In addition, the impact of W self-sputtering for the divertor erosion rises from $R^{\text{gross}}_{\text{W}\to\text{W}} \simeq 87.27 \times 10^{18}$ W-atoms s^{-1} to $R^{\text{gross}}_{\text{W}\to\text{W}} \simeq 118.45 \times$

Table 3. Surface-integrated W erosion rates for the case when the far-SOL temperature is constantly extrapolated to the wall. Positive and negative values for the dataset *net* denote net deposition and net erosion, respectively. It is noted that W erosion by D is dominated by CXNs.

(10^{18} atoms s^{-1})	net	gross	D → W	Ar → W	W → W
Main chamber	–43.44	122.64	27.58	65.84	29.22
Divertor	36.41	382.22	—	263.76	118.45

10^{18} W-atoms s^{-1} (increase of about 36%), which comes from an absolutely higher W influx from the main chamber. The slight increase in Ar sputtering results again from the previously explained statement that parts of the divertor top are within the extrapolation domain. The relative impact of the main chamber source further increases in the most conservative case of flat temperature profiles considered here. Though the divertor W gross source is still a factor of 3 larger than the main chamber, this is considerably less than for 2 eV far-SOL temperatures, where the ratio is given by 10.

Figure 13 infers a higher level of re-deposition especially on the low-field side of the machine, which can be seen by a lighter reddish shading in areas where erosion is dominated by CXN. However, it is worth mentioning that the transport matrix only predicts a small reduction in the W transport from the main chamber into the divertor with respect to both previous cases (here it is about 39%). Since the electron temperature does not surpass $I^{\text{W}}_{\text{pot}}$ in wide areas of the machine at all and it is still only marginally above $I^{\text{W}}_{\text{pot}}$ in the remaining areas, this is not entirely surprising. Consequently, the current plasma background makes it difficult to judge when the observed decoupling between net erosion and net deposition zones resulting from the significant non-local W transport diminishes and in how far these net erosion zones are critical in view of first wall lifetime. In order to address related questions, an extended-grid SOLPS-ITER plasma background could give more valuable insights. Finally, one can see the emergence of a net erosion zone at the lower end of the high-field side wall.

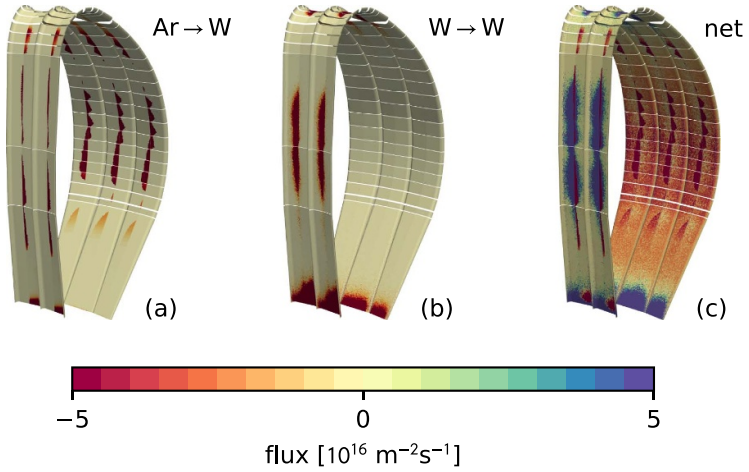

Figure 13. Tungsten main chamber ((*a*) and (*b*)) gross and (*c*) net erosion. The gross erosion is divided into the contributing species (*a*) Ar ions and (*b*) W self-sputtering. Positive values (shades of green and blue) indicate deposition, negative values (shades of red) indicate erosion. The far-SOL main chamber temperature profiles are constantly extended from the last available SOLPS-ITER flux tube towards the first wall.

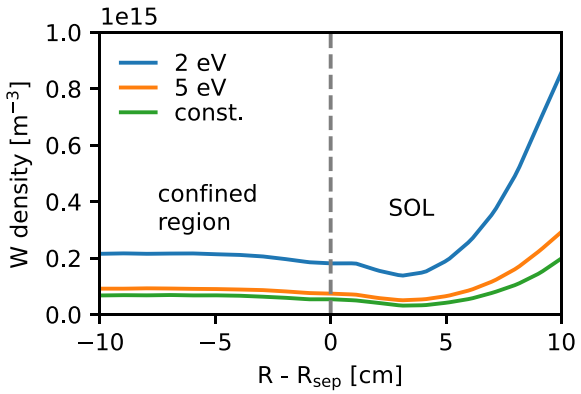

Figure 14. Radial W density profiles at the outer mid-plane for all three discussed cases. The separatrix position at the outer mid-plane is indicated by the grey dashed line.

3.4. Tungsten density profiles

Radial W density profiles at the outer mid-plane are given in figure 14. On the one hand, the figure reveals that the amount of W reaching the separatrix scales inversely with the far-SOL temperature, so that the highest W density, and thus also highest W influx, is expected for the coldest far-SOL temperature assumption discussed here (blue solid curve). For instance, W densities of the order of 2×10^{14} m^{-3} can be observed in the 2 eV case, which is a factor 2.4 and 3.3 higher compared to the values observed for the cases of 5 eV and constantly extrapolated temperature profiles in the far SOL, respectively. This inverse scaling can be explained once more with long ionization mean free paths that govern W SOL transport in the main chamber plasma and result in a shift of the ionization front closer to the separatrix.

On the other hand, almost constant W density profiles can be seen in the confined region in all cases, so that W transport is not suppressed in the pedestal. Of course, this is directly related to the assumption of constant anomalous diffusion throughout SOL and pedestal without accounting for any transport barrier. Correspondingly, the predictions on W influxes into the confined region are only a rough estimate and require more careful investigations in the future. This includes the use of spatially inhomogenous transport profiles, for instance to mimic the transport barrier, and the coupling of ERO2.0 to more sophisticated core transport models such as JINTRAC as reported in [4].

4. Conclusions

Tungsten erosion, re-deposition, and migration was modeled with the ERO2.0 code for the EU-DEMO tokamak taking into account the realistic geometry of PFCs in three dimensions. The plasma scenario was based on the only available SOLPS-ITER solution, which was generated for the 2017 magnetic Baseline equilibrium. Therefore, the simulation results are only of preliminary nature and not necessarily indicative for predictions on the full power operation in EU-DEMO. Indeed, they should be seen rather as a demonstration that the general workflow is established and should be used in the same time to diagnose critical aspects in terms of accurate predictions on the lifetime of PFCs. For instance, large gaps between the last flux surface on the SOLPS-ITER grid and the first wall panels were identified to introduce large uncertainties into the far-SOL plasma conditions. In order to estimate their impact on W erosion and transport, three different far-SOL plasma temperature profiles were considered here. Corresponding ERO2.0 simulations revealed that main chamber W erosion by D CXN gains in importance the colder the far-SOL plasma is. It even became the dominant erosion process for the case of the lowest temperature cut-off. To account for the increasing importance of D CXN on the W source, D CXN energy distribution at 12 different poloidal locations were imported from dedicated EIRENE modeling. For the present conditions, the advanced

approach was shown to give a broader but reduced W source around the outer mid-plane in comparison to the simplified mean energy approach. Beyond to D CXN, main chamber W erosion was also attributed to Ar ions (seeding impurity) and W self-sputtering in the ERO2.0 simulations. Contrary to CXN, their contribution gained in importance with increasing far-SOL temperature. In fact, Ar ions were identified to be the driving main chamber erosion process followed by W self-sputtering for the hottest case of flat temperature profiles from the B2-grid up to the wall. On the other side, W gross erosion of the divertor was dominated by seeded Ar ions for all three cases. The relative contribution of W self-sputtering increased with increasing temperature, but never contributed more than 1/3 to the divertor source.

A fundamental difference compared to prior ERO2.0 modeling for a full-W ITER as a proxy for EU-DEMO [25] could be observed regarding the transport of W. While only marginal transport from the main chamber into the divertor has been reported before, significant transport into the divertor was detected for all cases discussed in the present study. The qualitative change could be explained by long ionization mean free paths of W atoms in the cold and thin far-SOL plasma. At the same time, the strong W transport into the divertor resulted in large net erosion zones across the main chamber first wall. Whether this becomes critical in terms of first wall lifetime will be studied in the future with more relevant plasma scenarios.

Acknowledgments

This work has been carried out within the framework of the EUROfusion Consortium, funded by the European Union via the Euratom Research and Training Programme (Grant Agreement No 101052200-EUROfusion). Views and opinions expressed are however those of the author(s) only and do not necessarily reflect those of the European Union or the European Commission. Neither the European Union nor the European Commission can be held responsible for them. The authors gratefully acknowledge computing time on the supercomputer JURECA [35] at Forschungszentrum Jülich under Grant no. cjiek43.

Appendix

The following table gives information on averaged net erosion and net deposition rates in $\mathrm{nm\,h^{-1}}$ evaluated for different region. In particular, the *top* region is defined by all surface cells of the main chamber with Z coordinates larger than 4.5 m. The *inboard* and *outboard* account for all surface cells with Z coordinates smaller than 4.5 m that are additionally located on the high-field and low-field side of the machine, respectively. Regarding the *divertor*, no distinction between low-field and high-field side is made. In addition, the average for net erosion is only computed in areas of net erosion. The same logic is applied to the averaged net deposition rate. Finally, it is noted that the values should be taken with care as the average can deviate quite significantly from local peak values due to large averaging zones accompanied by a large spread in the actual values.

Table 4. Averaged net erosion and net deposition rates in $\mathrm{nm\,h^{-1}}$.

	$\langle\Gamma_{\mathrm{ero}}\rangle$ ($\mathrm{nm\,h^{-1}}$)			$\langle\Gamma_{\mathrm{depo}}\rangle$ ($\mathrm{nm\,h^{-1}}$)		
	2 eV	5 eV	const.	2 eV	5 eV	const.
Top	0.2	0.2	0.3	2.7	2.1	1.7
Inboard	0.4	4.2	13.6	1.1	2.3	5.5
Outboard	1.5	1.5	1.6	4.3	4.7	4.2
Divertor	5.3	4.7	0.4	9.6	15.9	27.3

ORCID iDs

C. Baumann 0000-0001-7712-5379
J. Romazanov 0000-0001-9439-786X
D. Matveev 0000-0001-6129-8427
A. Kirschner 0000-0002-3213-3225
F. Subba 0000-0002-8170-4792
S. Wiesen 0000-0002-3696-5475
S. Brezinsek 0000-0002-7213-3326
Ch. Linsmeier 0000-0003-0404-7191

References

[1] Kirschner A., Philipps V., Winter J. and Kögler U. 2000 *Nucl. Fusion* **40** 989
[2] Romazanov J. *et al* (JET Contributors) 2017 *Phys. Scr.* **T170** 014018
[3] Romazanov J. *et al* 2019 *Nucl. Mater. Energy* **18** 331–8
[4] Kumpulainen H.A., Groth M., Brezinsek S., Casson F., Corrigan G., Frassinetti L., Harting D. and Romazanov J. (JET contributors) 2024 *Plasma Phys. Control. Fusion* **66** 055007
[5] Romazanov J. *et al* 2020 *Contrib. Plasma Phys.* **60** e201900149
[6] Romazanov J. *et al* 2021 *Nucl. Mater. Energy* **26** 100904
[7] Romazanov J. *et al* 2022 *Nucl. Fusion* **62** 036011
[8] Federici G., Biel W., Gilbert M.R., Kemp R., Taylor N. and Wenninger R. 2017 *Nucl. Fusion* **57** 092002
[9] Federici G., Holden J., Baylard C. and Beaumont A. 2021 *Fusion Eng. Des.* **173** 112959
[10] Litaudon X. *et al* 2022 *Plasma Phys. Control. Fusion* **64** 034005
[11] Federici G., Baylard C., Beaumont A. and Holden J. 2021 *Fusion Eng. Des.* **173** 112960
[12] Maviglia F. *et al* 2020 *Fusion Eng. Des.* **158** 111713
[13] Siccinio M., Graves J.P., Kembleton R., Lux H., Maviglia F., Morris A.W., Morris J. and Zohm H. 2022 *Fusion Eng. Des.* **176** 113047
[14] Subba F., Coster D.P., Moscheni M. and Siccinio M. 2021 *Nucl. Fusion* **61** 106013
[15] Firdaouss M., Riccardo V., Martin V., Arnoux G. and Reux C. 2013 *J. Nucl. Mater.* **438** S536–9
[16] Stangeby P.C. 1987 *J. Phys. D: Appl. Phys.* **20** 1472
[17] Cornelissen M.J.H., Vernimmen J.W.M., Verstappen J.D.E., Zoethout E., Classen I.G.J., Beckers J. and Morgan T.W. 2025 *Nucl. Fusion* **65** 026009
[18] Stangeby P.C. 2000 *The Plasma Boundary of Magnetic Fusion Devices* (CRC Press)

[19] Lisgo S.W., Kukushkin A., Pitts R.A. and Reiter D. 2013 *J. Nucl. Mater.* **438** S580–4
[20] Schmid K., Mayer M., Adelhelm C., Balden M. and Lindig S. (ASDEX Upgrade Team) 2010 *Nucl. Fusion* **50** 105004
[21] Borodin D. *et al* 2014 *Phys. Scr.* **2014** 014057
[22] Kirschner A., Wienhold P., Philipps V., Coad J.P., Huber A. and Samm U. 2004 *J. Nucl. Mater.* **328** 62–66
[23] Mutzke A. and Schneider R. and Eckstein W. and Dohmen R. and Schmid K., von Toussaint U. G. B. 2019 SDTrimSP version 6.00 (https://doi.org/10.17617/2.3026474)
[24] Reiter D., Baelmans M. and Börner P. 2005 *Fusion Sci. Technol.* **47** 172–86
[25] Eksaeva A., Kirschner A., Romazanov J., Brezinsek S., Linsmeier C., Maviglia F., Siccinio M. and Ciattaglia S. 2022 *Phys. Scr.* **97** 014001
[26] Matveev D. *et al* 2024 *Nucl. Fusion* **64** 106043
[27] Rode S., Romazanov J., Reiser D., Brezinsek S., Linsmeier C. and Pukhov A. 2022 *Contrib. Plasma Phys.* **62** e202100172
[28] Reiser D., Reiter D. and Tokar M.Z. 1998 *Nucl. Fusion* **38** 165
[29] Harting D., Reiser D., Rode S., Romazanov J., Börner P., Feng Y., Frerichs H. and Knieps A. 2025 *Nucl. Mater. Energy* **42** 101887
[30] Homma Y. and Hatayama A. 2012 *J. Comput. Phys.* **231** 3211–27
[31] Di Genova S. *et al* 2023 *Nucl. Mater. Energy* **34** 101340
[32] Pitts R.A. *et al* 2025 *Nucl. Mater. Energy* **42** 101854
[33] Dekeyser W. *et al* 2021 *Nucl. Mater. Energy* **27** 100999
[34] Campbell-Miller M.D. and Simard B. 1996 *J. Opt. Soc. Am. B* **13** 2115–20
[35] Jülich Supercomputing Centre 2021 *J. Large-Scale Res. Facil.* **7** A182